Article

Operando X-ray Diffraction Studies of the Mg-Ion Migration Mechanisms in Spinel Cathodes for Rechargeable Mg-Ion Batteries

Liang Yin, Bob Jin Kwon, Yunyeong Choi, Christopher J. Bartel, Mengxi Yang, Chen Liao, Baris Key, Gerbrand Ceder, and Saul H. Lapidus*

Read Online

| ACCESS | Metrics & More | Article Recommendations | Supporting Information |

ABSTRACT: A promising high-voltage spinel oxide cathode material $MgCrMnO_4$ with 18% Mg/Mn inversion was synthesized successfully. A new custom operando battery device was designed to study the cation migration mechanisms of the $MgCrMnO_4$ cathode using 0.1 M $Mg(TPFA)_2$ electrolyte dissolved in triglyme and activated carbon as the anode. For the first time in multivalent batteries, high-quality operando diffraction data enabled the accurate quantification of cation contents in the host structure. Besides the exceptional reversibility of 12% Mg^{2+} insertion in $Mg_{1-x}CrMnO_4$ ($x \leq 1$), a partially reversible insertion of excess Mg^{2+} during overdischarging was also observed. Moreover, the insertion/extraction reaction was experimentally shown to be accompanied by a series of cation redistributions in the spinel

framework, which were further supported by density functional theory calculations. The inverted Mn is believed to be directly involved in the cation migrations, which would cause voltage hysteresis and irreversible structural evolution after overdischarging. Tuning the Mg/Mn inversion rate could provide a direct path to further optimize spinel oxide cathodes for Mg-ion batteries, and more generally, the operando techniques developed in this work should play a key role in understanding the complex mechanisms involved in multivalent ion insertion systems.
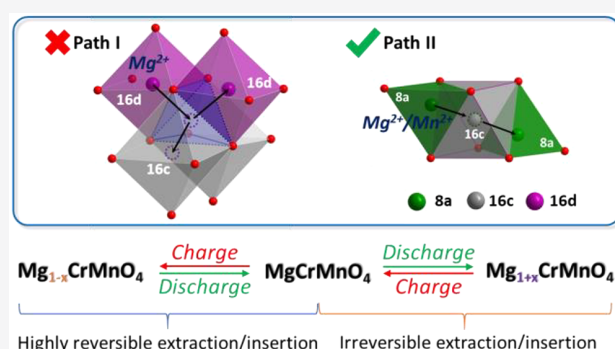
1. INTRODUCTION

Rechargeable Mg-ion batteries (MIBs) have attracted considerable attention as potential candidates for next-generation energy storage systems, especially for large-scale applications, mainly due to the massive abundance of Mg on earth and the high volumetric energy density of metallic Mg.[1] In the 2000s, Aurbach reported the first successful prototype of MIBs by assembling the Mo_6S_8 Chevrel phase as a cathode, metallic Mg as an anode, and $Mg(AlCl_2BuEt)_2$ as an electrolyte.[2] Although the reported energy density is relatively low due to the low operating voltage, this MIB system exhibited low polarization and excellent cycling stability with <15% capacity loss after 2000 cycles. Since then, a substantial body of work has been devoted to the search for functional Mg-based electrode materials and electrolytes operating at high potentials.[3–5] Because transition metals generally hybridize less with O^{2-} than with S^{2-} or Se^{2-}, one expects oxides to have higher potentials, as evidenced by density functional theory (DFT) calculations.[6] However, this higher potential is traded off with poorer diffusion kinetics for the Mg^{2+} ion and higher interfacial charge-transfer resistance, usually resulting in low electrochemical activity and reversibility of Mg^{2+} insertion and a large polarization between the anodic and cathodic reactions for most oxide cathodes. Therefore, significant effort is still needed

to understand the electrochemical mechanisms related to Mg^{2+} insertion in oxides in order to efficiently design high-voltage MIB cathode materials.

Spinel oxides (MgM_2O_4, M = V, Cr, Mn, Fe, Co, Ni, etc.) are promising high-voltage cathode materials for the reversible insertion of Mg^{2+}.[7] Though the migration of Mg^{2+} within the spinel host structure was discovered more than half a century ago,[8,9] the feasibility of spinel oxides as insertion hosts for Mg^{2+} has only recently been studied both theoretically and experimentally.[7,10–15] However, the mobility of Mg^{2+} in spinel oxides is generally still low and spinel oxides also suffer from cation disordering, further complicating their design. Studies on $MgMn_2O_4$[9,14,16,17] have indicated that this material is prone to Mg/Mn inversion, in which the octahedral sites (16d) are partially occupied by Mg^{2+} cations and the tetrahedral sites (8a) are partially occupied by Mn cations, accompanied by the disproportionation of Mn^{3+} (16d) into Mn^{2+} (on 8a) and Mn^{4+}
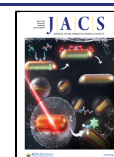
(on 16d) (Figure 1 left). This cation inversion is difficult to eliminate during synthesis because this structural disorder is
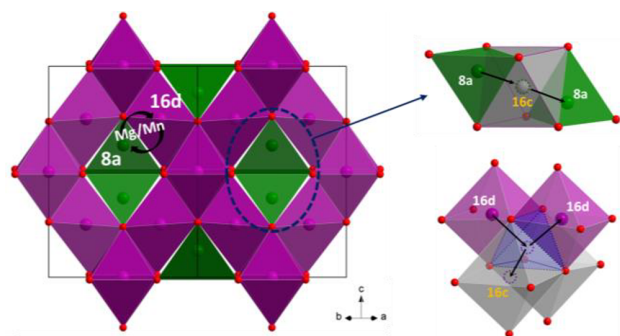
Figure 1. $MgCrMnO_4$ crystal structure (space group Fd-$3m$) with 16d octahedra shown in purple, vacant 16c octahedra shown in gray, and 8a tetrahedra shown in green. The possible diffusion pathways of Mg^{2+} (8a), Mg^{2+} (16d), and Mn^{2+} (8a) are shown on the right, in which right edges of the 16c octahedron are colored in purple indicating the edge sharing with 16d octahedra.

thermodynamically favorable due to an increase in configurational entropy. The detrimental effects of inversion defects on Mg^{2+} migration have been demonstrated by DFT calculations and confirmed experimentally.[14,15] Besides studies on the influence of cation inversion on Mg^{2+} migration, the phase evolution of the spinel upon Mg^{2+} extraction has also been investigated through ex situ X-ray powder diffraction on samples treated with acid digestions.[18,19] An intermediate phase, $Mg_{0.5}Mn_2O_4$, was observed, which suggested a two-phase process during the extraction of Mg^{2+}. In addition, rock-salt phases (space group Fm-$3m$) were observed when excess Mg^{2+} was inserted into $MgMn_2O_4$ and $MgCr_2O_4$ electrochemically, based on which the "intercalation and push-out" mechanism was proposed.[20] Recently, a complex spinel to rock-salt phase transition behavior during the Mg^{2+} insertion into $MgMn_2O_4$ was reported by ex situ techniques.[21] However, from the crystallographic point of view, a change in the lattice symmetry from spinel (space group Fd-$3m$) to rock-salt (space group Fm-$3m$) requires a random distribution of both Mg and transition metals (TMs) on two octahedral sites (16c and 16d), which is difficult to achieve by the "intercalation and push-out" process. It is instead highly possible that rock-salt phases are decomposed byproducts, such as MgO or TM oxide. Therefore, the understanding of phase evolution in spinel cathodes remains elusive, especially regarding the behavior of the site-inverted cations, Mn^{2+} (8a) and Mg^{2+} (16d). As shown in Figure 1, the inverted Mg^{2+} (16d) could plausibly be mobile by hopping between either 16d—16d sites or 16d—16c sites connected by the face-shared unoccupied tetrahedral site. The further optimization of spinel cathodes for Mg^{2+} demands a comprehensive and fundamental understanding of the migration mechanisms of all mobile cations $(Mg^{2+}$ and $Mn^{2+})$ and the corresponding evolution of the host structure.

Operando X-ray diffraction (XRD) is one of the most popular and well-developed advanced characterization techniques for the investigation of Li-ion and Na-ion battery systems during electrochemical processes.[22] The usage of the operando techniques can eliminate several potential issues of ex situ measurements, such as sample contaminations, structural relaxations, and inconsistencies between different ex situ

cells. In addition, operando XRD is extremely well-suited for the Mg-ion system due to the scattering physics of X-rays, which provide an enhanced sensitivity to Mg compared to Li or Na.[23] Thus, both atomic positions and contents of Mg cations can be accurately identified through XRD. Despite this, operando studies on the Mg battery system have been rarely reported.[24] Challenges of such studies include the strong scattering from the metallic Mg anode and the elevated battery operation temperature needed to ensure a reasonable electrochemical reaction rate during the measurement time. To the best of our knowledge, operando techniques have not yet been applied to study Mg-based spinel oxide cathodes for MIBs. In the present work, a custom cell device was built for the operando synchrotron XRD of the spinel cathode, $MgCrMnO_4$, in a rechargeable MIB using the weakly scattering activated carbon anode. The solid-solution of Cr and Mn in the spinel lattice has been shown to yield high Mg-ion activity while alleviating incompatibility with electrolytes and suppressing both Jahn—Teller distortion and Mg/TM inversion.[11] In this work, Mg/Mn inversion, phase evolution during electrochemical cycling, cation migration mechanisms, and Mg capacity were studied in detail through the combination of operando XRD and DFT calculations.

2. EXPERIMENTAL SECTION

Synthesis. $MgCrMnO_4$ was synthesized by using a sol—gel method similar to the previously reported preparation route.[11] Magnesium acetate tetrahydrate $(Mg(CH_3COO)_2 \cdot 4H_2O$, product no. M5661 in Sigma-Aldrich), chromium acetate hydroxide $(Cr_3(CH_3CO_2)_7(OH)_2$, product no. 318108 in Sigma-Aldrich), and manganese acetate dihydrate $(Mn(CH_3COO)_3 \cdot 4H_2O$, product no. 215880 in Sigma-Aldrich) were used as precursors, and citric acid $(C_6H_8O_7$, product no. C0759 in Sigma-Aldrich) was introduced as a capping agent. 12.5 mmol of precursors and 25.0 mmol of citric acid were dissolved in 200 mL of deionized water and stirred vigorously for 30 min at room temperature. The mixture was then heated at 120 °C to evaporate water until the solid powder was obtained. The resultant powders were calcined at 950 °C for 24 h in air and cooled down to room temperature naturally inside the furnace.

Structural Characterization. High-resolution synchrotron XRD data were collected at the high-resolution powder diffractometer beamline 11-BM at the Advanced Photon Source (APS) of Argonne National Laboratory $(\lambda = 0.412834$ Å). The powder sample was loaded in 0.8 mm diameter Kapton capillaries and measured with a multianalyzer detector system. Time-of-flight (TOF) neutron powder diffraction data were collected at the NOMAD powder diffraction beamline at the Spallation Neutron Source (SNS) of Oak Ridge National Laboratory. About 150 mg of powder was packed into a 3 mm diameter quartz capillary. The data collection time was 120 min. The NOMAD data were reduced using custom beamline software.[25] Rietveld refinements of the crystal structure were carried out using the TOPAS software package (Bruker-AXS, v6).

Operando Synchrotron X-ray Diffraction. The Mg-ion cell, which consists of the as-prepared $MgCrMnO_4$ cathode laminate and the activated carbon anode with a 0.1 M $Mg(TPFA)_2$ $([TPFA]^- = [(Al(OC(CF_3)_3)_4)^-])$ electrolyte dissolved in triglyme, was prepared for operando studies. The cathode slurry consisted of the active material, carbon black (C45, Timcal), and PVDF binder in a weight ratio of 6:2:2 in N-methylpyrrolidone (Sigma-Aldrich). The slurry was then cast on a stainless-steel foil and dried under vacuum at 80 °C to evaporate the solvent. The loading level of active material in the dry electrode was adapted to around 4 mg/cm². The electrodes were then punched into 1/8 in. disks, resulting in a thickness of ~50 μm. The electrolyte of 0.1 M $Mg[TPFA]_2$ dissolved in triglyme was prepared in an argon-filled glovebox, which has shown sufficient thermal and anodic stability for high-temperature electrochemistry.[26] The high specific surface area of the activated carbon gives rise to sufficient

double-layer charging to match the charge needed to cycle the cathode.[27] Glass fiber (1 μm pore size, Whatman GF/B) was used as the separator; its thickness was measured to be 0.68 mm prior to use.

Operando diffraction studies were carried out in a custom cell design inspired by the previously reported RATIX cell.[28] Photographs and a schematic drawing of the custom operando cell setup are shown in Figure S1. The cell body was cut from a quartz tube with an inner dimeter of 4 mm and thickness of 1 mm. Two stainless steel cylindrical rods (McMaster-Carr, 1/4 in. O.D.) were used to hold the cathode-separator-anode film in the center and also to provide the electrical contact. A constant pressure on the cell components is maintained by a closed, flat end stainless steel spring. Both ends of the quartz tube were sealed with 316 stainless steel caps (Swagelok, for 1/4 in. O.D. tubing) and graphite ferrules (Restek, 1/4 in. I.D.). The resistance wires were wrapped on the outer wall of the quartz tube to provide heating. The body of the cell device was covered with Kapton tape to avoid temperature fluctuations. A sample stage with three-dimensional printed insulating parts was constructed with Thor Lab parts to hold the cell, heating elements, and thermometer. The operando cell was assembled in an argon-filled glovebox and installed on a hexapod sample stage at the 11-ID-B beamline of the APS using a wavelength of 0.2114 Å, as shown in Figure S1b. The size of the beam was focused to 5×250 μm (vertical × horizontal). Diffraction data were collected on a PerkinElmer amorphous silicon-based area detector (2048×2048 pixels with 200 μm sides) at 0.1 s subframe time and a total acquisition time of 1 s per image.

A Maccor 4300 cycler was used to control the current or potential of the cell. Electrochemical cycling was carried out at 95 °C. The operation temperature was optimized in our previous work to increase the mobility of Mg^{2+} and minimize the decomposition of the organic electrolyte.[11] The cell was cycled galvanostatically at a constant current of C/20 (calculated using a nominal cathode capacity of 280 mAh/g, corresponding to a current of 4.43 μA) within a voltage range of −1.4−1.5 V vs activated carbon. A maximum charging and discharging time of 25 h was set to avoid continuous consumption of the electrolyte.

The two-dimensional X-ray scattering images were integrated using GSAS-II.[29] Data from a CeO_2 powder standard in a 1.1 mm diameter capillary mounted next to each cell were used for calibration. Modeling of diffraction patterns was carried out using the TOPAS software (version 6, Bruker AXS). In addition to peaks from the main spinel oxide cathode, the contribution from Fe was modeled as separate phases using the Pawley method.

Sequential Rietveld refinements were applied to extract structural information from the integrated one-dimensional operando diffraction patterns using Python codes. Since the cathode material kept the same cubic Fd-$3m$ phase during cycling, the identical structural model was applied, while structural parameters, including lattice parameters, atomic occupancies at 8a, 16c, 16d sites, atomic coordinates of oxygen, and isotropic displacement parameters were refined. However, it is difficult to differentiate changes in Mg and Mn contents at the same crystallographic site because one Mn is approximately equivalent to two Mg in terms of the cross-section of X-ray scattering, which is the real quantity probed in XRD. To simplify the interpretation of cation contents on each crystallographic site, only changes of Mg^{2+} contents at 8a, 16c, and 16d sites were refined, which are x, y, and z in $[Mg_{0.82-x}Mn_{0.18}]^{8a}[Mg_y]^{16c}[CrMn_{0.82}Mg_{0.18-z}]^{16d}O_4$. The refined change of the Mg^{2+} content is in reality equivalent to the actual changes both Mg and TM cations in terms of X-ray scattering power. The initial structural model for the sequential Rietveld refinement was generated from the fitting on the diffraction data collected before cycling. Then, the thermal displacement parameters and the amount of Mg/Mn inversion (x in $[Mg_{1-x}Mn_x]^{8a}[CrMn_{1-x}Mg_x]^{16d}O_4$) were fixed for all the following refinements. The structural model for the next new XRD pattern was generated from the refinement on the previous pattern.

Density Functional Theory Calculations. Calculations in this work use density functional theory (DFT) as implemented in the Vienna Ab Initio Simulation Package,[30,31] with the projector augmented-wave method,[32,33] and the generalized gradient approximation (GGA) as formulated by Perdew, Burke, and Ernzerhof (PBE).[34] For all calculations, the energy cutoff was set to 520 eV, and at least 1000 k-points were used per reciprocal atom. For geometry optimizations, energies were converged to 5×10^{-5} eV for electronic steps and 0.01 eV/Å for ionic steps.

Supercells of the tetragonal spinel ($I4_1/amd$) $MgCrMnO_4$ with 32 oxygen ions were used for all calculations. The cell shape and volume were allowed to optimize during relaxations, but an initially tetragonal cell was used to allow for potential Jahn−Teller distortions. Low-energy electrostatic configurations were sampled at various inversion rates and Mg concentrations to order Mg and Mn on the tetrahedral 8a site, and Mg, Mn, and Cr on the octahedral 16d site. In total, 110 different configurations were calculated with varying concentrations of Mg vacancies ($x = 0, 0.125, 0.25, 0.375, 0.5$) and inversion rates ($i = 0, 0.125, 0.25, 0.375, 0.5$). Note that because Cr is redox-inactive[11,12] and Mn is not expected to oxidize beyond 4+, the system is limited to $x + i \leq 0.5$.

The climbing image nudged elastic band (NEB) method[35] was used to calculate Mg and Mn migration energies. The barriers were calculated in the supercell with 32 oxygen ions based on a previous study on $MgMn_2O_4$ showing that the interaction between periodic images becomes negligible for that cell size.[15] Excluding initial and final end points, seven intermediate images were generated to capture the energy along the migration trajectory. For the NEB images, energies were converged to 5×10^{-4} eV for electronic steps and 0.01 eV/Å for ionic steps. The midpoint (16c site) of the migration path between 8a sites was reoptimized following the NEB calculation to more accurately obtain the site energy difference between the 8a and 16c site.

The Materials Project database[36] and pymatgen library[37] were used to set up and analyze the calculations in this work.

3. RESULTS AND DISCUSSION

Structural Characterization. Spinel oxide, $MgCrMnO_4$, is a thermodynamically stable phase and was directly synthesized by sol−gel. The Bragg diffraction peaks of the high-resolution synchrotron X-ray powder diffraction pattern (Figure 2) for the as-synthesized sample was indexed using the typical spinel cubic structure (space group Fd-$3m$, no. 227), with a lattice parameter of $a = 8.37738(1)$ Å. No evidence of phase impurities was observed. The sharp and symmetric Bragg peaks indicate that the spinel phase is a homogeneous solid-solution with good crystallinity. The amount of Mg/TM inversion was quantified through Rietveld refinements against X-ray and neutron powder diffraction data independently. Considering the difficulty to distinguish Mn and Cr in the X-ray powder diffraction due to their similar X-ray scattering powers, complementary Rietveld analyses of X-ray and neutron powder diffraction data were utilized to identify and quantify Mg/TM inversion, since the neutron scattering lengths of Cr (3.635 fm) and Mn (−3.73 fm) are substantially different.[38] The transition-metal species involved in cation inversion can therefore be identified due to the different scattering physics of X-rays and neutrons. Finally, the degree of inversion (x in $[Mg_{1-x}TM_x]^{8a}[TM_{2-x}Mg_x]^{16d}O_4$, TM = Cr and Mn) is 18.33(8)% refined from XRD data and 18.76(8)% refined from ND data when assuming that only Mn (and not Cr) could occupy the 8a site (Table S1). The exceptional agreement between the values refined from two individual data sets confirms the inversion of Mg/Mn instead of Mg/Cr in the $MgCrMnO_4$ sample. The inversion level is much lower than that of $MgMn_2O_4$ synthesized under similar conditions,[14] which indicates the role of Cr^{3+} in suppressing Mg/Mn inversion. Therefore, the actual composition of the $MgCrMnO_4$ sample can be rewritten as
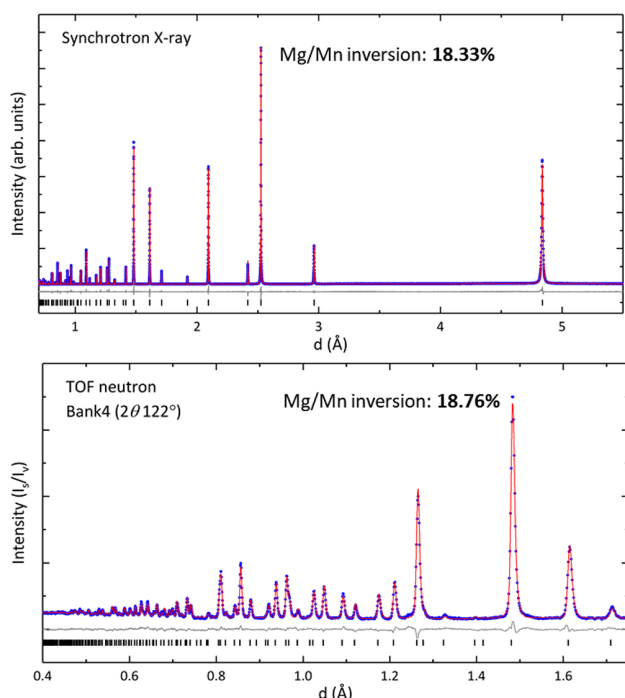
Figure 2. Individual Rietveld refinements against synchrotron XRD data (top) and TOF neutron diffraction data (bottom). Experimental data are shown as blue dots, the refined model is shown as a red line, the difference curve is shown in gray, and the positions of Bragg diffraction peaks are labeled with black tick marks.

$[Mg_{0.82}Mn_{0.18}]^{8a}[CrMn_{0.82}Mg_{0.18}]^{16d}O_4$. The details of the method and the refined crystallographic parameters are presented in the Supporting Information.

Operando Synchrotron X-ray Measurements. Based upon the detailed characterization of the pristine material, operando synchrotron XRD measurements were performed at

95 °C, utilizing a custom battery device described in the Experimental Section. As a demonstration of the high quality of the XRD data and the reliability of structural parameters that can be extracted from this data, a Rietveld refinement against the XRD data collected before cycling is shown in Figure S2. The presence of Fe metal reflections indicates imperfections in the alignment of the battery device along the X-ray beam direction. More than 30 Bragg peaks of the $MgCrMnO_4$ phase out to ~0.78 Å in d-spacing show sufficiently good signal/noise ratio and limited overlap with Fe peaks, which is sufficient to allow for detailed structural analysis of the cathode. The Mg/Mn inversion refined from the XRD data is 18%, which is in strong agreement with the values obtained by characterizing the pristine powder sample. Therefore, the high quality of XRD data obtained from the operando setup and the improved sensitivity of XRD to Mg ions, compared to Li or Na ions, enable accurate and reliable quantification of cation migrations in the spinel host structure during cycling through the Rietveld method.

The waterfall plot of the XRD data collected during the operando measurement, including the first charge/discharge cycle and partial second charging are shown in Figure 3 with the corresponding voltage profile on the left. The voltage curve of the operando cell is in good agreement with our previous ex situ measurements using commercial Swagelok cells operated at the same temperature.[11] The major Bragg peaks of each XRD pattern can be indexed using the same cubic spinel phase (space group Fd-3m). No inactive spinel phase or new rock-salt phase is observed, indicating that the $MgCrMnO_4$ cathode undergoes a homogeneous solid-solution reaction throughout the electrochemical measurement. Any structural changes on the surface cannot be detected by the Bragg diffraction due to the limited coherent length. Therefore, the investigations of the structural evolution in this study focus on the bulk structure of $MgCrMnO_4$. Since the bulk cathode material remains in the cubic spinel structure, only three crystallographic sites are involved in cation migration: one tetrahedral
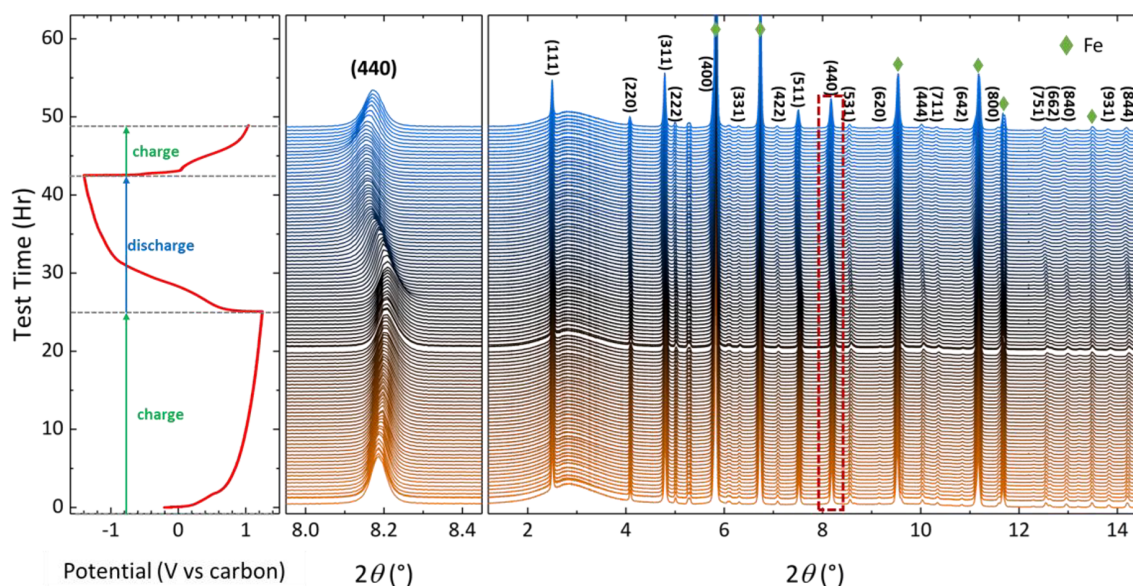
Figure 3. Operando synchrotron XRD patterns collected during charge/discharge at a rate of 4.43 μA at 95 °C with the Miller indices labeled in black and Fe peaks marked with blue diamond marks. The left panel shows the representative galvanostatic cycling profile (V vs activated carbon). The middle panel shows an enlargement of the (440) diffraction peak of spinel phase.
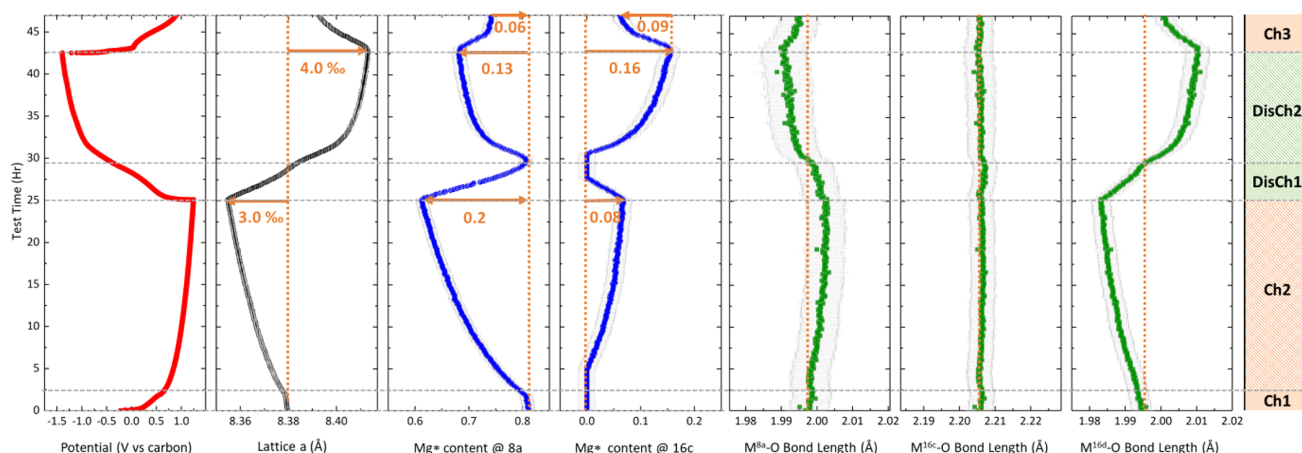
Figure 4. Structural parameters (lattice parameter, Mg* contents, and M−O bond lengths) from Rietveld refinements against operando XRD data with the electrochemical curve (V vs activated carbon) on the left. The Mg* contents at 8a and 16c sites are x and y in $[Mg_xMn_{0.18}]^{8a}[Mg_y]^{16c}[CrMn_{0.82}Mg_{0.18}]^{16d}O_4$, respectively. Ch1, Ch2, DisCh1, DisCh2, and Ch3 correspond to five stages of structural evolutions during the operando measurement.

site (8a) and two octahedral sites (16c and 16d), as shown in Figure 1. Tracking changes of cation contents on these three sites can provide information on the cation migration mechanisms. The operando XRD data were analyzed by means of sequential Rietveld refinements, in which the unit cell dimension, atomic positions, and occupations of the spinel structure were extracted. As mentioned above, both transition metals and Mg cations can potentially migrate during electrochemical cycling. However, it is impossible to differentiate changes of different cation species at the same crystallographic site by XRD. Therefore, a simplified model was applied to the interpretation of cation contents on each crystallographic site. Only the atomic occupancy of Mg^{2+} ions was refined during Rietveld refinements, thus a change in refined Mg content actually represents changes of all cation (Mg and Mn cations) present at that crystallographic site. This equivalent Mg content is labeled as the Mg* content. Details about the refinement procedures are given in the Experimental Section. Representative Rietveld refinements of the operando data at selected states-of-charge are shown in Figure S3. The refined structural parameters, such as the lattice parameter (a), Mg* contents, and M−O bond lengths, are plotted in Figure S4a.

Clear correlations of the lattice parameter, contents of Mg*, and M−O bond lengths with the voltage profile confirm the activity of the spinel oxide as a Mg^{2+} insertion cathode during cycling. Among these parameters, the Mg* content at 16d shows relatively small variations compared to the error bars. Additional sequential refinements were conducted by keeping the Mg* content at the 16d site constant while refining the remaining structural parameters. As shown in Figure S4b, the variations of other structural parameters are nearly the same no matter whether the Mg* occupancy at the 16d site was refined or not. Thus, the Mg* content at the 16d remains nearly unchanged during cycling, which indicates that cations (inverted-Mg, Mn, Cr) occupying the 16d site are immobile. The inactivity of the inverted Mg^{2+} could be ascribed to the high migration barrier. As shown in Figure 1, Mg^{2+}@16d has to migrate through a small triangular face (3.55 Å²) to the adjacent unoccupied 8a tetrahedral site. In contrast, the triangular face through which Mg^{2+}@8a migrates to the 16c site is ∼30% larger (4.54 Å²). Therefore, the following

discussions focus on cation migrations through 8a and 16c sites. The structural parameters obtained from the Rietveld refinements with constant cation contents on 16d are shown in Figure 4.

The first charge/discharge cycle can be categorized in four stages (Ch1, Ch2, Disch1, Disch2), as labeled in Figure 4. In the Ch1 stage, the spinel cathode shows little activity since the lattice size and cation occupancies remain nearly unchanged during the first 2 h of charging. The initial capacity of the cell is mainly attributed to side reactions. Once the battery is charged to ∼0.7 V (vs activated C), a substantial decrease in the lattice parameter was observed. Meanwhile, both Mg* content at 8a and the M^{16d}−O bond length decrease, indicating the removal of cations from the tetrahedral 8a site accompanied by the oxidation of TMs at the 16d site. As such, a successful extraction reaction was observed. After charging for another 2 h in the Ch2 stage, in addition to removing cations from the 8a site, the Mg* content at 16c increases steadily, indicating that cations start to accumulate on the 16c site along the tet(8a)−oct(16c)−tet(8a) hopping pathway. The increased occupation of cations on the 16c octahedral site can be attributed to the decreased repulsion between 8a and 16c sites when more vacancies are generated on the 8a site during charging. The possibility of cation occupation at 16c will be discussed later in further detail through theoretical calculations. At the end of Ch2, ∼0.2 Mg* were removed from the 8a tetrahedral site with 40% of them remaining on the octahedral 16c site. This result shows that 0.12 Mg* can be deintercalated from the spinel structure at the end of first charging, corresponding to ∼34 mAh/g with a small volume shrinkage (−0.88%). Since the reversible migration of Mn^{2+} between the tetrahedral 8a site and octahedral 16c site has been reported in the Mn_3O_4 cathode for Li-ion batteries,[39] the Mn cations on 8a sites could also participate in the cation migrations in addition to Mg^{2+}. Thus, the actual amount of deintercalated cations (Mg + Mn) could be even smaller than 0.12 mol per $MgCrMnO_4$. However, the measured electrochemical capacity has already exceeded the theoretical capacity of $MgCrMnO_4$ (∼280 mAh/g) at the end of charging. A substantial fraction of the extra delivered capacity is attributed to side reactions, such as the oxidative decomposition of the electrolyte.

To avoid continuous consumption of the electrolyte, the operando battery was forced to discharge after charging for 25 h. Once the battery began to discharge, the lattice size increased with synchronous changes to Mg* contents at 8a and 16c sites. The discharge process can be separated into two stages (DisCh1 and DisCh2). During the first discharge stage, DisCh1, the Mg*(8a) content increased, while the Mg*(16c) content decreased, indicating that those cations accumulated on the 16c site are migrating back to the 8a site. The increment of the Mg*(8a) content is larger than the decrement of the Mg*(16c) content, confirming that extra Mg cations were indeed inserted into the spinel framework (i.e., >1 Mg per CrMnO$_4$ unit). At the end of DisCh1 (discharged to −0.4 V), the 16c site is unoccupied, and the Mg* content at the 8a site is restored to that of the pristine state. Moreover, the lattice parameter and M−O bond lengths at three sites are also nearly fully recovered. A direct comparison of the diffraction patterns collected at the pristine state and the end of Disch1 (Figure S5) shows that peak positions, intensities, and widths of the spinel phase are nearly identical. Therefore, the removal/insertion of Mg^{2+} in the spinel oxide is exceptionally reversible, and the integrity of the bulk MgCrMnO$_4$ cathode is unchanged during the Ch1−Ch2−DisCh1 sequence. In addition, the highly reversible structural evolution also confirms that the potential migration of Mn cations between 8a and 16c sites is reversible, and the removal of Mn cations from the spinel lattice is infeasible due to the very different X-ray scattering between Mn and Mg.

The battery was further discharged. During the second discharge stage (DisCh2), the continued increase of the M^{16d}−O bond length is observed, indicating further reduction of TMs. This reduction was accompanied by synchronous changes of Mg* contents at 8a and 16c sites. The increase of the Mg* content at 16c is larger than the decrease of Mg* content at 8a, suggesting the insertion of excess Mg^{2+} into the fully recovered MgCrMnO$_4$ cathode. The insertion of Mg^{2+} during overdischarging is accompanied by internal cation migrations between the 8a and 16c sites. Once inserted Mg^{2+} begins occupying the empty 16c site, the large repulsion between Mg^{2+} on the 16c site and the faced-shared 8a site forces cations from occupying the 8a site to the adjacent unoccupied 16c sites. At the end of DisCh2 (−1.4 V), approximately 0.03 additional Mg^{2+} were inserted into the fully discharged MgCrMnO$_4$ cathode and 0.13 Mg* migrate from 8a sites to 16c sites with a 1.2% expansion in the cell volume, which is much larger than the cell volume shrinkage during charging. This cation rearrangement is why the discharged MgCrMnO$_4$ cathode showed significant lattice expansion compared with that of the pristine state in previous ex situ studies.[11]

After discharging to −1.4 V, the battery was charged for a second cycle (Ch3). Operando data were collected for only part of Ch3 due to limited beam time. As shown in Figure 4 during Ch3, the lattice size of the spinel phase decreases, while the Mg* content on the 8a site increases and the Mg* content on the 16c site decreases, confirming the activity of the overdischarged cathode. After charging for 4.5 h, 0.06 Mg* migrate back from the 16c site to the 8a site, and 0.03 Mg* were removed from the spinel lattice. Interestingly, the amount of extra Mg* inserted into the spinel structure during overdischarging was also 0.03. The difference is that the removal of 0.03 Mg* does not restore the cathode back to the pristine state. Therefore, the insertion/extraction chemistry of

Mg$_{1+x}$CrMnO$_4$ ($x \leq 0.03$) during DisCh2 and Ch3 is irreversible, which could be attributed to the migration of inverted Mn cations. It is possible that Mn cations on the 8a site could be pushed to empty 16c sites, which are only partially occupied by extra Mg^{2+}. Then, hysteresis occurs from either the migration of Mn cations back to 8a sites or the removal of Mn cations from the spinel during the second charging.

The above analyses based on the operando XRD data clearly map out the structural evolutions and cation migrations of the MgCrMnO$_4$ cathode during electrochemical cycling. The insertion/extraction chemistry of the MgCrMnO$_4$ cathode is accompanied by a series of cation redistributions over 8a and 16c sites, while keeping the 16d site unchanged. However, the structural evolution does not proceed at "uniform speed" during cycling. The insertion reaction slows down after charging to 0.7 V during Ch2 and after discharging to −1.0 V during DisCh2, with the rate of cell voltage change always decreasing steadily. This mismatch between the structural evolution and the electrochemical behavior is the outcome of the oxidative (and reductive) decomposition of the electrolyte. The level of accessible content of Mg^{2+} in the MgCrMnO$_4$ cathode is highly limited by the narrow window of the electrolyte.

Ab Initio Calculations. DFT calculations were performed to better understand the structural transformations occurring during charging and discharging. Spinel structures were sampled with varying levels of inversion, i, and concentrations of Mg, x, where i refers to the fraction of Mn present on the 8a site, and x refers to the number of Mg present per CrMnO$_4$ unit. As the experimental refinement (Figure 1) indicates that only Mn (and not Cr) inverts, Cr was restricted to the 16d site for all calculations.

Understanding Mg/Mn Inversion. As shown in Figure 1, the measured Mg/Mn inversion rate for the as-synthesized sample is ∼18%. To understand the origin of this inversion rate in MgCrMnO$_4$, we calculated the relative energies of various orderings of Mg and Mn on the 8a and 16d sites and Mg, Mn, and Cr on the 16d sites. In Figure 5a, we show the energy of the spinel compound at varying levels of inversion (i in [Mg$_{1-i}$Mn$_i$]^{8a}[CrMn$_{1-i}$Mg$_i$]^{16d}O$_4$. The minimum energy is found for an inversion rate of 37.5%, larger than that observed experimentally (∼18%). The thermodynamics of inversion can be considered as a trade-off between two effects: Mg generally prefers octahedral coordination thereby favoring inversion; however, Mn also prefers the octahedral site, in particular when its formal valence is +3 or +4. In Figure S7, we show the calculated magnetic moments of the transition metals as a function of inversion. The results show that Mn is 3+ in the 16d site when no inversion is present, but each inverted Mn results in disproportionation into Mn^{2+} on the 8a site and Mn^{4+} on the 16d site. Inversion is restricted by the energy required to create this Mn^{2+} in the tetrahedral site, which is balanced by the energy lowering associated with moving Mg into an octahedral site. DFT in the GGA-PBE approximation (PBE) overestimates the stability of Mn charge disproportionation as can be seen by comparing the calculated reaction energy,[40] ΔE_{rxn}, for MnO + MnO$_2$ → Mn$_2$O$_3$ ($\Delta E_{rxn,PBE}$ = −0.47 eV/Mn$_2$O$_3$) to the experimental reaction enthalpy at 298 K ($\Delta H_{rxn,exp}$ = −0.52 eV/Mn$_2$O$_3$).[41] We see that PBE overstabilizes this disproportionated state by ∼25 meV/Mn. In Mg$_x$CrMnO$_4$, this leads to the higher predicted inversion rate compared with what was observed experimentally.
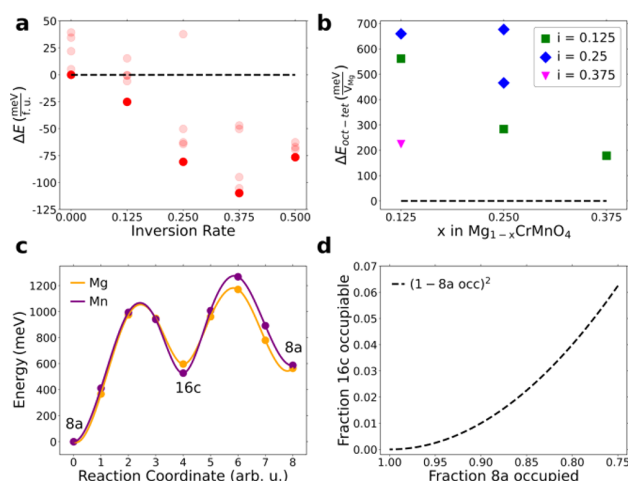
Figure 5. (a) Energies relative to the pristine (zero inversion) $MgCrMnO_4$. At each inversion rate, several cation orderings were sampled, with the lowest energy shown by the fully shaded circles. Energies are normalized per $MgCrMnO_4$ formula unit (f.u.). (b) Comparing the energy of Mg extraction from either the 8a site (tet) or 16d site (oct) at varying levels of inversion, i. Energies are normalized per Mg extracted (V_{Mg}) from the Mg_xCrMnO_4 supercell with 32 oxygen anions. Positive values indicate a preference for removal from the tetrahedral site. (c) NEB pathway for vacancy-mediated diffusion along the 8a−16c−8a trajectory for Mg and Mn cations. (d) The fraction of 16c sites that are occupiable, as defined by being surrounded by two 8a vacancies, as a function of 8a occupation.

Mg Removal. The maximum fraction of Mg that can be removed from Mg_xCrMnO_4 is dictated by the inversion rate, i, and the maximum oxidation states of Cr and Mn. In Figure S7, we show the magnetic moments of Cr and Mn as a function of inversion and Mg concentration up to 50% of the theoretical capacity ($x = 0.5$) and find that Cr is redox-inactive (remaining 3+) and Mn oxidation is limited to 4+. Because Mn can only be 2+ on the tetrahedral 8a site, the only oxidation that can charge-compensate for Mg removal must occur on Mn^{3+} on the 16d site, limiting the maximum available capacity to be 0.32 Mg per $CrMnO_4$ unit (~88 mAh/g), as there are 0.64 Mn^{3+} cations in $MgCrMnO_4$ when it has 18% inversion (and two Mn^{3+} must be oxidized per Mg^{2+} removed). In principle, Mg can be removed from either the 8a site or the 16d site, but the operando studies show that charging is commensurate with a depletion of the 8a occupancy only. In Figure 5b, we compare the calculated energies of various inverted structures with Mg removed from either the 8a or 16d sites and find that removal from the 8a site is always energetically preferred. This is consistent with the preference for Mg to reside on the octahedral 16d site, if available.

Site Occupations upon Charging. The operando results shown in Figures 3 and 4 show a complex evolution of site occupancies upon charging, including partial occupation of the octahedral 16c site. DFT calculations can help reveal which ions are responsible for the observed diffraction signals at each site. To understand the occupation of the 16c site and determine which ions are mobile during charging, we performed NEB calculations to estimate the migration energy of Mg and Mn. In Figure 5c, we show the energy along the path for Mg and Mn migration between 8a sites through the vacant 16c site when 25% inversion is present and 0.25 Mg is removed. Mobility calculations were performed at 25%

inversion, as an intermediate value between the ~18% inversion observed experimentally, and the inversion rate calculated to be lowest in energy (37.5%). Both Mg and Mn show similar migration barriers, suggesting both cations may be mobile from the 8a site. In Figure S9 and Table S2, we show the effect of local and nonlocal environments on the migration barrier to be small, suggesting the reported mobilities are not overly sensitive to the inversion rate. Further, the migration path shown in Figure 5c suggests that the energy of occupying a 16c site that is surrounded by 8a vacancies can be comparable to the energy of occupying an 8a site that is surrounded by 16c vacancies, suggesting the plausibility of 16c occupation. The limited occupation of 16c of ~8% at the end of Ch2 likely arises from the low fraction of vacant 8a sites in the spinel structure. Because 16c and 8a are face-sharing, it is unlikely that neighboring 8a and 16c sites can both be occupied due to the high repulsion between cations. Therefore, the occupation of 16c requires the two neighboring 8a sites to be vacant. Based on this idea, we evaluated the maximum fraction of occupiable 16c sites with three assumptions: (1) that 8a and 16c sites have equal occupation probability; (2) cations cannot occupy two face-shared sites (i.e., neighboring 8a and 16c sites); and (3) the spinel structure is maintained during charging. With these assumptions, because two neighboring empty 8a sites enable one occupiable 16c site (between them), the fraction of occupiable 16c sites is equal to $(1 − 8a$ site occupancy$)^2$, as shown in Figure 5d. As Mg is removed from the 8a site during charging, the probability of a 16c site being surrounded by 8a vacancies (and therefore occupiable), as estimated under these assumptions, grows to ~4% at the experimentally observed maximum capacity of 0.2 Mg, which is within the error range of the measured 16c occupancy during Ch2 (Figure 3). It should be noted that this is a simple model that does not account for the relative energetics of the various configurations and only counts the number of 16c sites that are available as a function of 8a occupation. Still, the NEB results and site probability analysis suggest that upon the removal of Mg ions from the 8a site, some small occupation of the 16c site by either Mg or Mn is plausible in the spinel structure.

Excess Mg during Overdischarge. The occupation of the 16c site during the discharge below −0.4 V (DisCh2) far exceeds the predicted upper limit of 16c site occupancy shown in Figure 5d. Because the 8a sites are fully occupied in $MgCrMnO_4$, additional Mg ions must fill the vacant 16c sites. The face-sharing nature of the 8a and 16c sites makes it energetically unfavorable to accommodate a cation/anion ratio >3:4 in the spinel structure. This energetic penalty can be relieved by the formation of a rock-salt-like phase in which all cations are on octahedral sites, as is the case for the lithiation of $LiMn_2O_4$ to $Li_2Mn_2O_4$.[42] In Figure S8, we show the relative stability of the spinel, in which the tetrahedral 8a site is occupied (and 16c is unoccupied), and rock-salt-like phase, in which the octahedral 16c site is occupied (and 8a is unoccupied). There are no stable rock-salt-like phases found on the convex hull at intermediate compositions compared to the normal spinel, $MgCrMnO_4$, and the overmagnesiated rock-salt phase with a 1:1 cation/anion ratio, Mg_2CrMnO_4. These results support two possible ideas: (1) the cathode phase undergoes a $MgCrMnO_4$/Mg_2CrMnO_4 two-phase reaction; and (2) other stable phases at intermediate compositions exist. The operando diffraction data clearly suggest a homogeneous solid-solution reaction during overdischarging, in which a
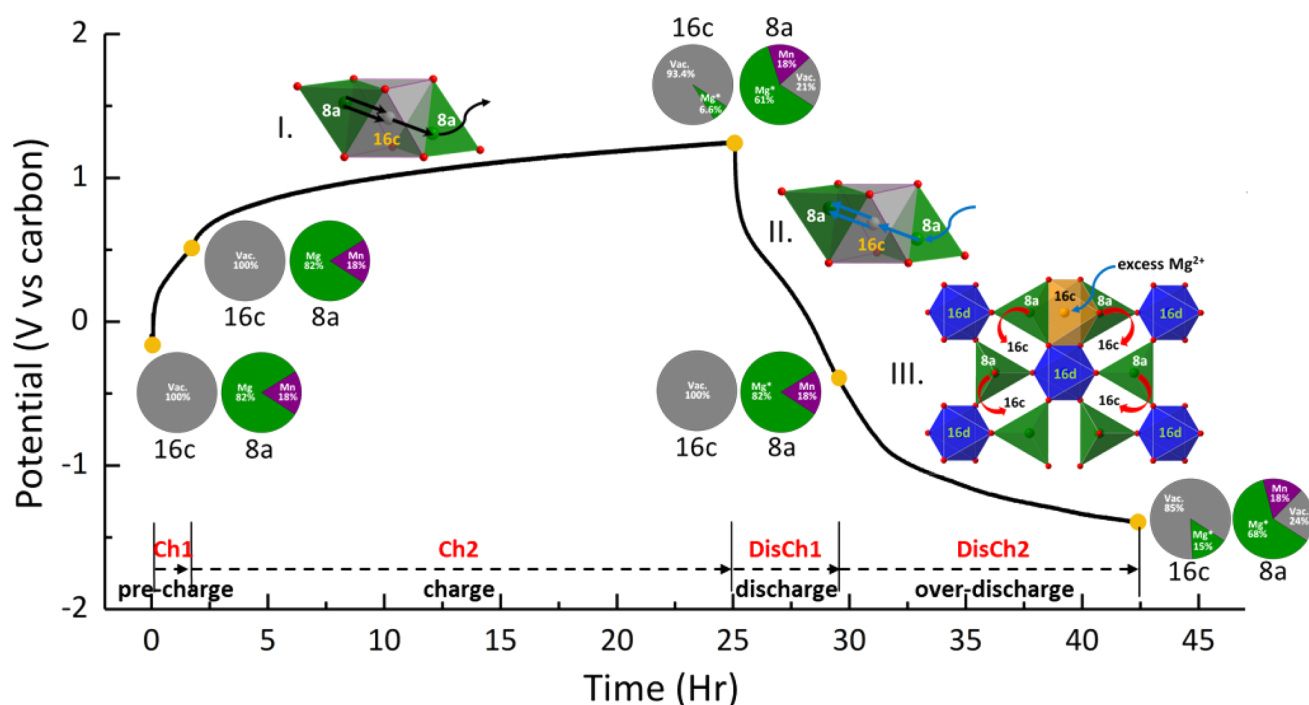
Figure 6. Schematic illustration of three cation migration processes of the inverted MgCrMnO$_4$ during the first charge/discharge. Pie charts represent the factions of cations on the 8a and 16c sites at the selected state of charge.

spinel-like phase with cations occupying both 8a and 16c sites is present.

The Mechanism of Cation Migrations in the Inverted MgCrMnO$_4$. A detailed microscopic and quantitative understanding of cation migrations in the MgCrMnO$_4$ cathode is made possible through the high-quality structural data provided by the operando synchrotron XRD experiment as well as the complementary ab initio calculations. A schematic summary of the structural evolution of MgCrMnO$_4$ cathode during cycling is shown in Figure 6. Taken together, we find that the spinel host structure is quite stable with the removal/insertion of Mg^{2+}. The insertion of Mg^{2+} is accompanied by two homogeneous solid-solution reactions involving cation redistributions among the tetrahedral 8a and octahedral 16c sites. These cation motions are driven by either vacancy on the 8a site during charging or the insertion of excess Mg^{2+} on the 16c site during overdischarging. Conversely, the transition metals and the inverted Mg^{2+} on the 16d sites remain immobile. The inverted Mn^{2+} not only affects the migration barrier for Mg^{2+}[15] but can also be mobile, as suggested by DFT calculations. Though the migration of Mn^{2+} during Ch2 and DisCh1 is hard to (dis)prove by the operando XRD data, the reversibility of the insertion reaction suggests that, if present, the migration of inverted Mn^{2+} is reversible without overdischarging. However, during overdischarge (DisCh2), the migration of Mn^{2+} was confirmed to be active and at least partially irreversible. The detrimental effect of irreversible Mn^{2+} migration was confirmed by the rapidly decreased rate of extraction at the end of Ch3. In addition, the large voltage hysteresis observed between charging and discharging could be ascribed to the asymmetric migration mechanisms of those inverted Mn cations. Therefore, besides the effects of Mg/Mn inversions on the activation energy for the diffusion of Mg^{2+},[15] the inverted Mn cations can join in cation migrations along the 8a−16c−8a diffusion pathway, which could directly affect the

insertion chemistry. Finally, it is encouraging to note that synthetic routes to reduce inversion results in an enhancement of the electrochemical performance,[11] which could provide a direct path to increase the reversibility of Mg 8a site occupancy upon cycling, as shown in this study.

4. CONCLUSIONS

In the present work, the electrochemical mechanism of MgCrMnO$_4$ as a cathode for MIBs is clarified through operando synchrotron XRD and ab initio calculations. A custom high-temperature battery device was built to carry out an operando XRD study of a Mg-based cathode at an elevated temperature. This device enables the collection of high-quality diffraction data for the accurate quantification of cation contents in cathodes, which is critical for understanding the complex mechanisms involved in Mg^{2+} (de)insertion. Moreover, the migration mechanisms of Mg^{2+} and inverted Mn^{2+} were resolved utilizing Rietveld refinements against the operando data. In the current cell configuration, the reversible extraction of 12% Mg^{2+} cations in MgCrMnO$_4$ was achieved, which indicates that the majority of the observed capacity can be ascribed to side reactions instead of insertion reactions. It is encouraging that the insertion chemistry of Mg$_{1−x}$CrMnO$_4$ ($x \leq 1$) is largely fully reversible. However, the continuous insertion of excess Mg^{2+} into MgCrMnO$_4$ is detrimental to its structural reversibility, which is likely ascribed to the irreversible migration of inverted Mn^{2+}. Therefore, tuning the Mg/Mn inversion rate offers the possibility of further optimizing spinel oxide cathodes for MIBs. This is the first time that the cation migration mechanism in a multivalent cathode is elucidated though the precise quantification of cation contents against operando diffraction data. This approach is generally applicable to study other battery materials and opens important routes to understanding and designing materials for energy storage applications.

ASSOCIATED CONTENT

Ⓢ Supporting Information

The Supporting Information is available free of charge at https://pubs.acs.org/doi/10.1021/jacs.1c04098.

Operando battery devices figures, representative fits to XRD data, and details of plots of additional figures and tables (PDF)

AUTHOR INFORMATION

Corresponding Author

Saul H. Lapidus − X-ray Science Division, Advanced Photon Source and Joint Center for Energy Storage Research, Argonne National Laboratory, Lemont, Illinois 60439, United States; ⊙ orcid.org/0000-0002-7486-4325; Email: slapidus@anl.gov

Authors

Liang Yin − X-ray Science Division, Advanced Photon Source and Joint Center for Energy Storage Research, Argonne National Laboratory, Lemont, Illinois 60439, United States; ⊙ orcid.org/0000-0001-5396-782X

Bob Jin Kwon − Chemical Sciences and Engineering Division and Joint Center for Energy Storage Research, Argonne National Laboratory, Lemont, Illinois 60439, United States; ⊙ orcid.org/0000-0001-7395-0814

Yunyeong Choi − Department of Materials Science and Engineering, University of California Berkeley, Berkeley, California 94720, United States

Christopher J. Bartel − Department of Materials Science and Engineering, University of California Berkeley, Berkeley, California 94720, United States; ⊙ orcid.org/0000-0002-5198-5036

Mengxi Yang − Chemical Sciences and Engineering Division and Joint Center for Energy Storage Research, Argonne National Laboratory, Lemont, Illinois 60439, United States

Chen Liao − Chemical Sciences and Engineering Division and Joint Center for Energy Storage Research, Argonne National Laboratory, Lemont, Illinois 60439, United States; ⊙ orcid.org/0000-0001-5168-6493

Baris Key − Chemical Sciences and Engineering Division and Joint Center for Energy Storage Research, Argonne National Laboratory, Lemont, Illinois 60439, United States; ⊙ orcid.org/0000-0002-1987-1629

Gerbrand Ceder − Department of Materials Science and Engineering, University of California Berkeley, Berkeley, California 94720, United States; Materials Sciences Division, Lawrence Berkeley National Laboratory, Berkeley, California 94720, United States; ⊙ orcid.org/0000-0001-9275-3605

Complete contact information is available at:
https://pubs.acs.org/10.1021/jacs.1c04098

Notes

The authors declare no competing financial interest.

ACKNOWLEDGMENTS

REFERENCES

(1) Canepa, P.; Sai Gautam, G.; Hannah, D. C.; Malik, R.; Liu, M.; Gallagher, K. G.; Persson, K. A.; Ceder, G. Odyssey of Multivalent Cathode Materials: Open Questions and Future Challenges. *Chem. Rev.* **2017**, *117* (5), 4287−4341.

(2) Aurbach, D.; Lu, Z.; Schechter, A.; Gofer, Y.; Gizbar, H.; Turgeman, R.; Cohen, Y.; Moshkovich, M.; Levi, E. Prototype systems for rechargeable magnesium batteries. *Nature* **2000**, *407* (6805), 724−7.

(3) Guo, Z.; Zhao, S.; Li, T.; Su, D.; Guo, S.; Wang, G. Recent Advances in Rechargeable Magnesium-Based Batteries for High-Efficiency Energy Storage. *Adv. Energy Mater.* **2020**, *10* (21), 1903591.

(4) Zhang, Y.; Geng, H.; Wei, W.; Ma, J.; Chen, L.; Li, C. C. Challenges and recent progress in the design of advanced electrode materials for rechargeable Mg batteries. *Energy Storage Mater.* **2019**, *20*, 118−138.

(5) Ponrouch, A.; Bitenc, J.; Dominko, R.; Lindahl, N.; Johansson, P.; Palacin, M. R. Multivalent rechargeable batteries. *Energy Storage Mater.* **2019**, *20*, 253−262.

(6) Rong, Z.; Malik, R.; Canepa, P.; Sai Gautam, G.; Liu, M.; Jain, A.; Persson, K.; Ceder, G. Materials Design Rules for Multivalent Ion Mobility in Intercalation Structures. *Chem. Mater.* **2015**, *27* (17), 6016−6021.

(7) Liu, M.; Rong, Z.; Malik, R.; Canepa, P.; Jain, A.; Ceder, G.; Persson, K. A. Spinel compounds as multivalent battery cathodes: a systematic evaluation based on ab initio calculations. *Energy Environ. Sci.* **2015**, *8* (3), 964−974.

(8) Radhakrishnan, N.; Biswas, A. A neutron diffraction study of the cation migration in $MgMn_2O_4$. *physica status solidi (a)* **1976**, *37* (2), 719−722.

(9) Rosenberg, M.; Nicolau, P. Electrical properties and cation migration in $MgMn_2O_4$. *Phys. Status Solidi B* **1964**, *6* (1), 101−110.

(10) Zhang, Y.; Liu, G.; Zhang, C.; Chi, Q.; Zhang, T.; Feng, Y.; Zhu, K.; Zhang, Y.; Chen, Q.; Cao, D. Low-cost $MgFe_xMn_{2-x}O_4$ cathode materials for high-performance aqueous rechargeable magnesium-ion batteries. *Chem. Eng. J.* **2020**, *392*, 123652.

(11) Kwon, B. J.; Yin, L.; Park, H.; Parajuli, P.; Kumar, K.; Kim, S.; Yang, M.; Murphy, M.; Zapol, P.; Liao, C.; Fister, T. T.; Klie, R. F.; Cabana, J.; Vaughey, J. T.; Lapidus, S. H.; Key, B. High Voltage Mg-Ion Battery Cathode via a Solid Solution Cr−Mn Spinel Oxide. *Chem. Mater.* **2020**, *32* (15), 6577−6587.

(12) Kwon, B. J.; Lau, K.-C.; Park, H.; Wu, Y. A.; Hawthorne, K. L.; Li, H.; Kim, S.; Bolotin, I. L.; Fister, T. T.; Zapol, P.; et al. Probing Electrochemical Mg-Ion Activity in $MgCr_{2-x}V_xO_4$ Spinel Oxides. *Chem. Mater.* **2020**, *32* (3), 1162−1171.

(13) Han, J.; Yagi, S.; Ichitsubo, T. Suppressive effect of Fe cations in $Mg(Mn_{1-x}Fe_x)_2O_4$ positive electrodes on oxidative electrolyte decomposition for Mg rechargeable batteries. *J. Power Sources* **2019**, *435*, 226822.

(14) Bayliss, R. D.; Key, B.; Sai Gautam, G.; Canepa, P.; Kwon, B. J.; Lapidus, S. H.; Dogan, F.; Adil, A. A.; Lipton, A. S.; Baker, P. J.; Ceder, G.; Vaughey, J. T.; Cabana, J. Probing Mg Migration in Spinel Oxides. *Chem. Mater.* **2020**, *32* (2), 663−670.

(15) Sai Gautam, G.; Canepa, P.; Urban, A.; Bo, S.-H.; Ceder, G. Influence of inversion on Mg mobility and electrochemistry in spinels. *Chem. Mater.* **2017**, *29* (18), 7918−7930.

(16) Malavasi, L.; Ghigna, P.; Chiodelli, G.; Maggi, G.; Flor, G. Structural and transport properties of $Mg_{1-x}Mn_xMn_2O_{4\pm\delta}$ spinels. *J. Solid State Chem.* **2002**, *166* (1), 171−176.

(17) Mănăilă, R.; Păuşescu, P. Structural changes in $MgMn_2O_4$ at high temperatures. *Phys. Status Solidi B* **1965**, *9* (2), 385−394.

(18) Ariyoshi, K.; Masuda, S. Mechanism of Mg extraction from $MgMn_2O_4$ during acid digestion. *Phys. Chem. Chem. Phys.* **2020**, *22* (8), 4677−4684.

(19) Knight, J. C.; Therese, S.; Manthiram, A. On the Utility of Spinel Oxide Hosts for Magnesium-Ion Batteries. *ACS Appl. Mater. Interfaces* **2015**, *7* (41), 22953−61.

(20) Okamoto, S.; Ichitsubo, T.; Kawaguchi, T.; Kumagai, Y.; Oba, F.; Yagi, S.; Shimokawa, K.; Goto, N.; Doi, T.; Matsubara, E. Intercalation and Push-Out Process with Spinel-to-Rocksalt Transition on Mg Insertion into Spinel Oxides in Magnesium Batteries. *Adv. Sci. (Weinh)* **2015**, *2* (8), 1500072.

(21) Tuerxun, F.; Otani, S.; Yamamoto, K.; Matsunaga, T.; Imai, H.; Mandai, T.; Watanabe, T.; Uchiyama, T.; Kanamura, K.; Uchimoto, Y. Phase Transition Behavior of $MgMn_2O_4$ Spinel Oxide Cathode during Magnesium Ion Insertion. *Chem. Mater.* **2021**, *33* (3), 1006−1012.

(22) Zhu, H.; Huang, Y.; Zhu, H.; Wang, L.; Lan, S.; Xia, X.; Liu, Q. In Situ Probing Multiple-Scale Structures of Energy Materials for Li-Ion Batteries. *Small Methods* **2020**, *4* (6), 1900223.

(23) Pecharsky, V.; Zavalij, P. *Fundamentals of powder diffraction and structural characterization of materials*; Springer Science & Business Media: New York, 2008; pp 211−214.

(24) Fu, Q.; Sarapulova, A.; Trouillet, V.; Zhu, L.; Fauth, F.; Mangold, S.; Welter, E.; Indris, S.; Knapp, M.; Dsoke, S.; Bramnik, N.; Ehrenberg, H. In Operando Synchrotron Diffraction and in Operando X-ray Absorption Spectroscopy Investigations of Orthorhombic V_2O_5 Nanowires as Cathode Materials for Mg-Ion Batteries. *J. Am. Chem. Soc.* **2019**, *141* (6), 2305−2315.

(25) Neuefeind, J.; Feygenson, M.; Carruth, J.; Hoffmann, R.; Chipley, K. K. The Nanoscale Ordered MAterials Diffractometer NOMAD at the Spallation Neutron Source SNS. *Nucl. Instrum. Methods Phys. Res., Sect. B* **2012**, *287*, 68−75.

(26) Lau, K.-C.; Seguin, T. J.; Carino, E. V.; Hahn, N. T.; Connell, J. G.; Ingram, B. J.; Persson, K. A.; Zavadil, K. R.; Liao, C. Widening electrochemical window of Mg salt by weakly coordinating perfluoroalkoxyaluminate anion for Mg battery electrolyte. *J. Electrochem. Soc.* **2019**, *166* (8), A1510.

(27) Yoo, H. D.; Jokisaari, J. R.; Yu, Y.-S.; Kwon, B. J.; Hu, L.; Kim, S.; Han, S.-D.; Lopez, M.; Lapidus, S. H.; Nolis, G. M.; et al. Intercalation of magnesium into a layered vanadium oxide with high capacity. *ACS Energy Lett.* **2019**, *4* (7), 1528−1534.

(28) Liu, H.; Allan, P. K.; Borkiewicz, O. J.; Kurtz, C.; Grey, C. P.; Chapman, K. W.; Chupas, P. J. A radially accessible tubular in situ X-ray cell for spatially resolved operando scattering and spectroscopic studies of electrochemical energy storage devices. *J. Appl. Crystallogr.* **2016**, *49* (5), 1665−1673.

(29) Toby, B. H.; Von Dreele, R. B. GSAS-II: the genesis of a modern open-source all purpose crystallography software package. *J. Appl. Crystallogr.* **2013**, *46* (2), 544−549.

(30) Botana, A. S.; Norman, M. R. Electronic structure and magnetism of transition metal dihalides: bulk to monolayer. *Phys. Rev. Materials* **2019**, *3* (4), 044001.

(31) Kresse, G.; Furthmüller, J. Efficiency of ab-initio total energy calculations for metals and semiconductors using a plane-wave basis set. *Comput. Mater. Sci.* **1996**, *6* (1), 15−50.

(32) Kresse, G.; Hafner, J. Norm-conserving and ultrasoft pseudopotentials for first-row and transition elements. *J. Phys.: Condens. Matter* **1994**, *6* (40), 8245.

(33) Blöchl, P. E.; Jepsen, O.; Andersen, O. K. Improved tetrahedron method for Brillouin-zone integrations. *Phys. Rev. B: Condens. Matter Mater. Phys.* **1994**, *49* (23), 16223.

(34) Perdew, J. P.; Burke, K.; Ernzerhof, M. Generalized Gradient Approximation Made Simple. *Phys. Rev. Lett.* **1996**, *77* (18), 3865−3868.

(35) Henkelman, G.; Jónsson, H. Improved tangent estimate in the nudged elastic band method for finding minimum energy paths and saddle points. *J. Chem. Phys.* **2000**, *113* (22), 9978−9985.

(36) Jain, A.; Ong, S. P.; Hautier, G.; Chen, W.; Richards, W. D.; Dacek, S.; Cholia, S.; Gunter, D.; Skinner, D.; Ceder, G.; Persson, K. A. Commentary: The Materials Project: A materials genome approach to accelerating materials innovation. *APL Mater.* **2013**, *1* (1), 011002.

(37) Ong, S. P.; Richards, W. D.; Jain, A.; Hautier, G.; Kocher, M.; Cholia, S.; Gunter, D.; Chevrier, V. L.; Persson, K. A.; Ceder, G. Python Materials Genomics (pymatgen): A robust, open-source python library for materials analysis. *Comput. Mater. Sci.* **2013**, *68*, 314−319.

(38) Sears, V. F. Neutron scattering lengths and cross sections. *Neutron news* **1992**, *3* (3), 26−37.

(39) Thackeray, M. M. Exploiting the Spinel Structure for Li-ion Battery Applications: A Tribute to John B. Goodenough. *Adv. Energy Mater.* **2021**, *11* (2), 2001117.

(40) Bartel, C. J.; Weimer, A. W.; Lany, S.; Musgrave, C. B.; Holder, A. M. The role of decomposition reactions in assessing first-principles predictions of solid stability. *npj Comput. Mater.* **2019**, *5* (1), 4.

(41) Barin, I.; Sauert, F.; Schultze-Rhonhof, E.; Sheng, W. S. *Thermochemical Data of Pure Substances*, 3rd ed.; VCH: New York, 1993; pp 1−963.

(42) Sun, X.; Yang, X.; Balasubramanian, M.; McBreen, J.; Xia, Y.; Sakai, T. In Situ Investigation of Phase Transitions of $Li_{1+y}Mn_2O_4$ Spinel during Li-Ion Extraction and Insertion. *J. Electrochem. Soc.* **2002**, *149* (7), A842−A848.